MATERIALS SCIENCE

Design metastability in high-entropy alloys by tailoring unstable fault energies

Xin Wang[1]†, Rafael Rodriguez De Vecchis[1]†, Chenyang Li[2]†, Hanlei Zhang[1], Xiaobing Hu[3], Soumya Sridar[1], Yuankang Wang[1], Wei Chen[2]*, Wei Xiong[1]*

Metastable alloys with transformation-/twinning-induced plasticity (TRIP/TWIP) can overcome the strength-ductility trade-off in structural materials. Originated from the development of traditional alloys, the intrinsic stacking fault energy (ISFE) has been applied to tailor TRIP/TWIP in high-entropy alloys (HEAs) but with limited quantitative success. Here, we demonstrate a strategy for designing metastable HEAs and validate its effectiveness by discovering seven alloys with experimentally observed metastability for TRIP/TWIP. We propose unstable fault energies as the more effective design metric and attribute the deformation mechanism of metastable face-centered cubic alloys to unstable martensite fault energy (UMFE)/unstable twin fault energy (UTFE) rather than ISFE. Among the studied HEAs and steels, the traditional ISFE criterion fails in more than half of the cases, while the UMFE/UTFE criterion accurately predicts the deformation mechanisms in all cases. The UMFE/UTFE criterion provides an effective paradigm for developing metastable alloys with TRIP/TWIP for an enhanced strength-ductility synergy.

INTRODUCTION

Developing alloys with a combination of high strength and ductility is the paramount goal in structural materials engineering. However, most strengthening mechanisms, such as precipitation and solid solution hardening, are detrimental to ductility (*1*, *2*). Metastability engineering (*3*, *4*) has been demonstrated to be an effective strategy to overcome the strength-ductility trade-off in ferrous alloys (*5*) by introducing interface hardening from a dual-phase structure and transformation- or twinning-induced plasticity (TRIP/TWIP). During deformation, martensite/twin formation provides alternative pathways for partial dislocations to glide, and the newly formed phase/twin boundary reduces the dislocation mean free path, leading to the dynamic Hall-Petch effect (*6*). Recently, metastability engineering has also been used in developing high-entropy alloys (HEAs) (*3*, *4*) that contain multiple principal elements (*7*–*11*). The concept of HEAs offers a vast composition space and brings a previously undiscovered path for developing advanced materials with promising properties, such as excellent corrosion resistance (*12*), high strength (*11*), and biocompatibility (*13*). In terms of the mechanical properties, the combination of "HEA effects," such as the severe lattice distortion and solid solution strengthening, and the metastable engineering leads to HEAs with high strength and excellent ductility (*14*). Nonetheless, the effective design of HEAs with desired microstructure and deformation mechanisms is still a formidable challenge.

HEAs represent a paradigm shift in materials research from the corner of phase diagrams to the central region of the high-dimensional phase space. Facing with the astronomical design space, the computational-aided design offers a more efficient way than the Edisonian approach for exploring composition-process-structure relationships in HEAs (*15*–*17*). For example, a variety of effective computational approaches, such as phenomenological parameters (*18*), machine learning models (*17*, *19*, *20*), and the calculation of phase diagrams (CALPHAD) method (*21*–*23*), have been applied to predict the HEA phases for a given composition. However, the competition of phase stabilities is a function of both alloy composition and the processing history, especially for metastable phases. As a result, the influence of heat treatment and phase transformations, such as the athermal martensitic transformation during quenching, should be addressed to achieve a higher prediction accuracy.

The competing deformation mechanisms in the face-centered cubic (fcc) phase, such as dislocation glide, twinning, and martensitic transformation, are usually determined by the intrinsic stacking fault energy (ISFE) (*14*, *21*). The ISFE is the excess energy associated with the formation of the ISF by the dissociation of a lattice dislocation $a_0/2<110>$ into two $a_0/6<112>$ partial dislocations (a_0 is the lattice constant) (*24*). In austenitic steels, TRIP prevails over TWIP when ISFE is lower than 20 mJ/m^2, and TWIP is found in alloys when the ISFE lies between 20 and 40 mJ/m^2 (*25*). However, this rule does not generalize to other alloys such as HEAs. For example, transmission electron microscopy (TEM) experiments found that $Co_{10}Cr_{10}Fe_{40}Mn_{40}$ has a low ISFE of 13 ± 4 mJ/m^2, but this HEA is a TWIP alloy (*26*). Moreover, recent studies have shown that the experiments tend to overestimate the ISFE in concentrated alloys (*24*), while the density functional theory (DFT) calculations can give negative ISFE values for TRIP HEAs (*27*, *28*), making the ISFE criterion impractical for rigorous alloy design and discovery. ISFE is the energy change after the stacking fault formation, but it does not necessarily correlate with the energy barrier for the martensite or twin formation process. A more in-depth understanding of the deformation-induced martensite/twin formation process and their energy barrier is thus critical. Previous experimental studies found that the formation of deformation twins is associated with the partial dislocation glide on every {111} plane in fcc materials, while hexagonal close-packed (hcp) martensite forms as the result of the movement of partial dislocations on every other {111} plane (*29*–*31*). Therefore, we introduce two intrinsic quantities: unstable martensite fault energy (UMFE) and unstable twin fault energy (UTFE). The differences between UMFE/UTFE and ISFE define the energy barrier for martensite/twin formation, which controls the competition between

[1]Physical Metallurgy and Materials Design Laboratory, Department of Mechanical Engineering and Materials Science, University of Pittsburgh, Pittsburgh, PA 15261, USA. [2]Department of Mechanical, Materials, and Aerospace Engineering, Illinois Institute of Technology, Chicago, IL 60616 USA. [3]Department of Materials Science and Engineering, Northwestern University, Evanston, IL 60208, USA.
*Corresponding author. Email: w-xiong@outlook.com (W.X.); wchen66@iit.edu (W.C.)
†These authors contributed equally to this work.

different deformation mechanisms and allows us to predict the TRIP/TWIP behaviors in HEAs.

Figure 1 illustrates our strategy for designing HEAs with the desired phase and deformation mechanism. First, we predict the phase stability using the CALPHAD method for more than 100,000 compositions of the Co-Cr-Fe-Mn-Ni system to screen single-phase fcc HEAs free of brittle intermetallics at the homogenization temperature of 1200°C. Then, we compute the energy difference between the fcc and hcp phases at room temperature to identify the alloys as either fcc single phase or fcc + hcp dual phases (Fig. 1B) because this energy difference describes the competition between these phases during quenching. Seven alloys with TRIP/TWIP were selected on the basis of the kernel density analysis (Fig. 1C) and their fcc stability compared with two reference alloys (Ref-1: $Co_{20}Cr_{20}Fe_{20}Mn_{20}Ni_{20}$ and Ref-2: $Co_{10}Cr_{10}Fe_{40}Mn_{40}$). Then, we calculate the energy differences UMFE–ISFE and UTFE–ISFE to understand the energy barrier for martensite and twin formation, respectively (Fig. 1D). The comparison of the unstable fault energy differences defined in this work is considered the new guidelines to introduce the TRIP/TWIP effects. Last, we validate the design by conducting experiments and identifying the relationship among alloying elements, stacking fault energies, and deformation mechanisms (Fig. 1E). Here, we demonstrate an effective design strategy for HEAs using metastable engineering. This work reveals that the UMFE-ISFE and UTFE-ISFE predict the martensite and twin formation better than ISFE, and the design strategy is successful (Fig. 1F).

RESULTS

Microstructure and fcc stability screening using thermodynamic modeling

An accurate database is necessary to perform a high-fidelity prediction on phase stability. We chose the latest HEA thermodynamic database, with all binary systems and 60% ternary systems assessed. Moreover, we evaluated the reliability of the CALPHAD modeling for HEAs by comparing experiments and model predictions to ensure that the calculation is accurate (Fig. 2, A and B). Figure 2A summarizes the accuracy of reported phase predictions using machine learning (*17*, *19*, *20*), CALPHAD (*19*, *22*), and phenomenological parameters (details in table S1) (*19*). The machine learning and CALPHAD approaches perform better than the phenomenological parameters (*19*). Both machine learning and CALPHAD approaches are not computationally intense methods. Although machine learning models reported in literature show a satisfactory accuracy, heat treatment conditions are often not considered as model inputs. Existing machine learning classification models were also not built to predict specific phases and phase fractions (*17*, *20*), which are essential for alloy design and discovery. On the contrary, the CALPHAD approach calculates the phase and their fraction for a given temperature and composition, and the phase accuracy can be further improved as the previous study did not consider the athermal phase transformation during cooling (*19*, *22*).

Because the primary product of martensitic transformation in fcc HEAs is the ε martensite with an hcp structure (*3*), the chemical

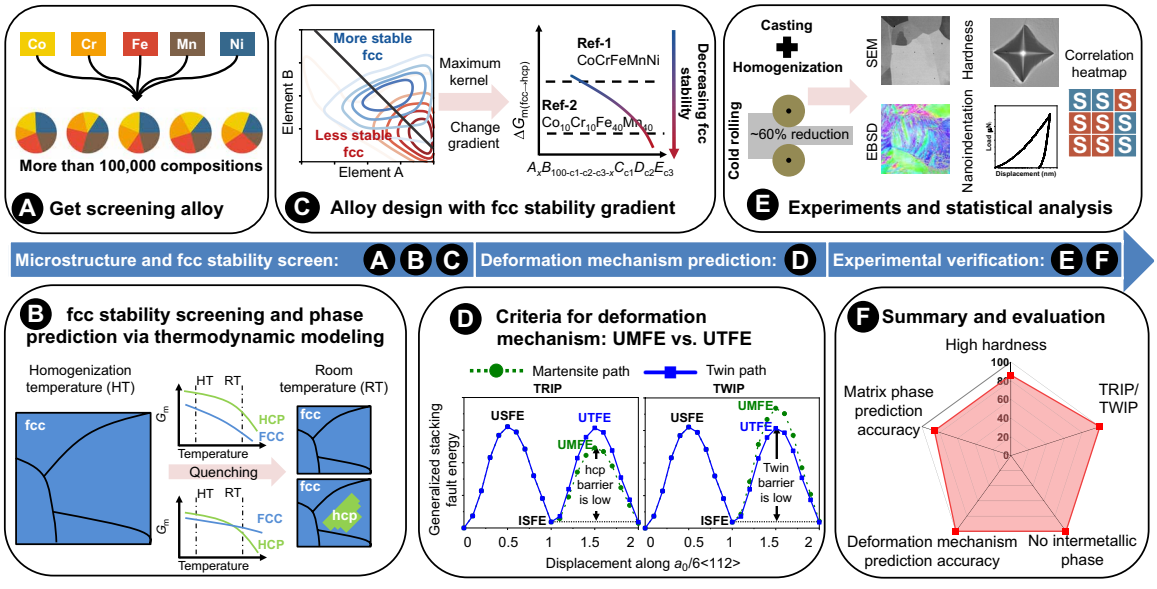

Fig. 1. Design workflow. (**A** to **C**) Schematics of the fcc stability and phase prediction via thermodynamic modeling. (A) Co, Cr, Fe, Mn, and Ni are mixed into the HEA, where element contents are in the range of 0 to 40 at %. (B) The phase at the homogenization temperature (1200°C) and room temperature are predicted via thermodynamic modeling. We only select alloys with a single fcc phase at 1200°C. If the Gibbs free energy of fcc is lower than the hcp at room temperature, then the alloy is labeled as an fcc single-phase alloy; otherwise, it is an fcc + hcp dual-phase alloy. (C) The Gibbs free energy difference between fcc and hcp for all compositions are compared with two reference alloys and are categorized into less stable fcc and more stable fcc. The alloys with the compositionally complementary elemental pairs that produce the maximum change of kernel density are identified, and seven alloys with a different fcc stability are chosen for further calculations. Because all designed alloys have a lower fcc stability than Ref-1 ($Co_{20}Cr_{20}Fe_{20}Mn_{20}Ni_{20}$), they will form martensite or twins after cold rolling. (**D**) Deformation mechanism prediction via DFT. USFE, ISFE, UMFE, and UTFE are unstable stacking fault energy, intrinsic stacking fault energy, unstable martensite fault energy, and unstable twin fault energy, respectively. We propose that if the energy barrier for martensite (hcp) formation (UMFE-ISFE) is smaller than the energy barrier for twinning (UTFE-ISFE), then the alloy is a TRIP alloy; otherwise, the alloy is TWIP dominant. (**E** and **F**) Design validation by experiments. (E) Schematics of the sample preparation, testing, characterization, and statistical analysis. (F) Evaluation of the design metrics. Designed alloys are shown as predicted secondary deformation mechanism and phases. More than 80% of the designed alloys have higher hardness compared with the reference HEA (Ref-2: $Co_{10}Cr_{10}Fe_{40}Mn_{40}$). EBSD, electron backscatter diffraction; SEM, scanning electron microscope.

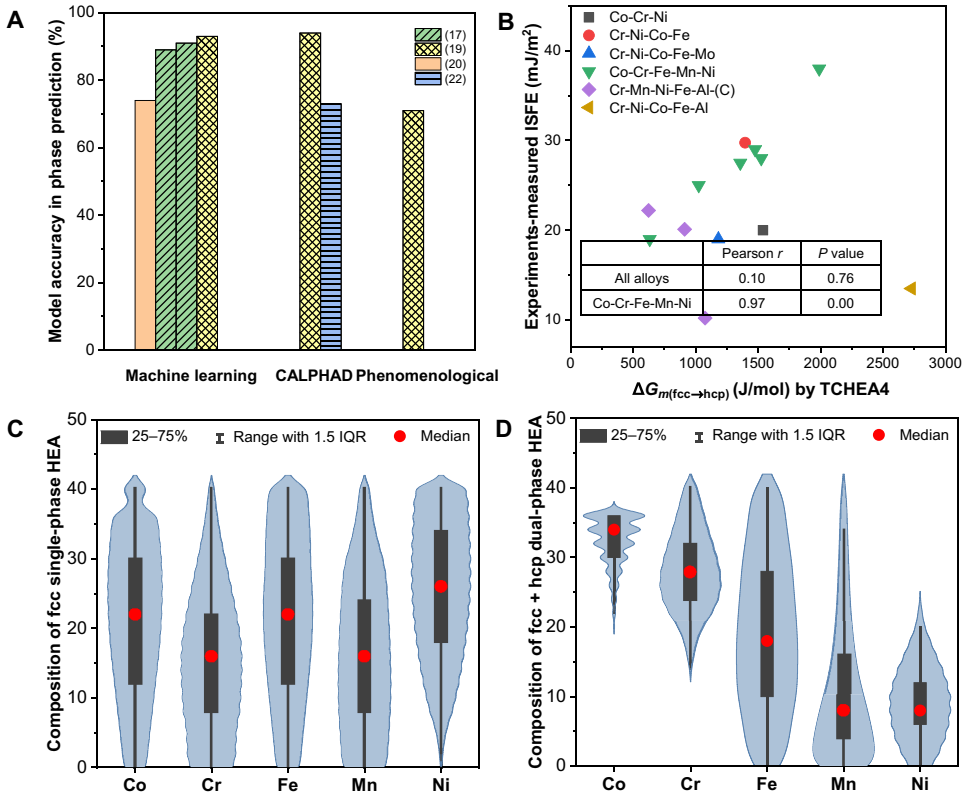

Fig. 2. Evaluation of the CALPHAD approach and thermodynamic model screening results. (**A**) Comparison of the phase prediction accuracy using machine learning, CALPHAD, and phenomenological parameter approaches based on literature, where the classification type, methods, and accuracy are available in table S1 (*17*, *19*, *20*, *22*). (**B**) Comparison of the experimentally measured ISFE (*33*–*40*) and the model-predicted value of the Gibbs free energy change of fcc-to-hcp transformation at room temperature. Each symbol represents a group of alloys containing the same elements, while there may be multiple data with different element content (details in table S2). The inset table shows the Pearson correlation coefficient *r* for all data and alloys containing Co, Cr, Fe, Mn, and Ni. (**C** and **D**) Screening results of $Co_xCr_yFe_{(100-x-y-z-w)}Mn_zNi_w$ ($0 \le x, y, z$, and w, $100-x-y-z-w \le 40$ atomic fraction), where the alloy compositions form single fcc at 1200°C. The width of the blue area represents the probability density of compositions corresponding to different alloying elements, and 1.5 IQR is 1.5 times the interquartile range (IQR). (C) The distribution of fcc single-phase alloy, which has a $\Delta G_{m(fcc\text{-}to\text{-}hcp)} > 0$ at 293 K. (D) The distribution of fcc + hcp dual-phase alloy, which has a $\Delta G_{m(fcc\text{-}to\text{-}hcp)} < 0$ at 293 K. The calculations of a few hundred compositions failed because of the numerical issue, and they were not included in the data visualization.

driving force of martensitic transformation can be expressed as the Gibbs energy change [$\Delta G_{m(fcc\text{-}to\text{-}hcp)}$] that corresponds to the thermodynamic model–predicted ISFE (*32*). Smaller $\Delta G_{m(fcc\text{-}to\text{-}hcp)}$ and ISFE indicate a lower fcc stability; i.e., it is easier for fcc to transform into hcp. We collected experimentally measured stacking fault energies (*33*–*40*), which usually have an uncertainty of about 5 mJ/m^2 (details in table S2), and compared them with the calculated $\Delta G_{m(fcc\text{-}to\text{-}hcp)}$ at room temperature (293 K) (Fig. 2B). On the basis of the Pearson correlation coefficient *r* for all alloy systems, the experimental ISFE and $\Delta G_{m(fcc\text{-}to\text{-}hcp)}$ show a very weak linear relationship because *r* is close to 0. Meanwhile, the *r* for Co-Cr-Fe-Mn-Ni alloy system (green triangles in Fig. 2B) is close to 1, and the *p*-value is smaller than 0.05. This result shows a statistically significant positive correlation between the experimental ISFE and the CALPHAD-calculated $\Delta G_{m(fcc\text{-}to\text{-}hcp)}$ for alloys containing Co, Cr, Fe, Mn, and Ni. Thus, the CALPHAD approach is reliable for predicting the fcc-to-hcp phase transformation in the Co-Cr-Fe-Mn-Ni systems.

Next, we performed a high-throughput screening of more than 100,000 compositions in the Co-Cr-Fe-Mn-Ni system. Compositions with a single fcc phase at the homogenization temperature (1200°C) were selected for further study. This screening criterion ensures that the phase composition is the same as the overall alloy composition, and no ductility degradation is caused by the formation of brittle intermetallic phases. Figure 2 (C and D) represents violin plots that show the elemental distribution of fcc single-phase [$\Delta G_{m(fcc\text{-}to\text{-}hcp)}$ at 293 K > 0] and fcc + hcp dual-phase [$\Delta G_{m(fcc\text{-}to\text{-}hcp)}$ at 293 K < 0] HEAs, respectively. We find that fcc single-phase HEAs have less dependency on any particular alloying element. However, the fcc + hcp dual-phase HEA is more likely to form with a high Co or Cr content and a limited addition of Mn or Ni.

It is widely accepted that lower ISFE, i.e., the decreasing fcc stability, leads to the deformation mechanisms switching from a pure dislocation glide to a combination of a dislocation glide and twinning followed by a dislocation glide together with martensitic transformation (*24*, *41*). Hence, identifying alloys with a gradient fcc stability could help design alloys with TRIP and TWIP effects. Two well-studied HEAs were used as the reference to guide our design. The first reference alloy is $Co_{20}Cr_{20}Fe_{20}Mn_{20}Ni_{20}$ HEA, which has a more stable fcc that only shows a deformation-induced twin after a severe (*42*) or low-temperature deformation (*10*). The second reference alloy is $Co_{10}Cr_{10}Fe_{40}Mn_{40}$ with a less stable fcc, which shows a TWIP during a room temperature deformation (*26*) and an hcp martensite formation after a high-pressure torsion (*43*) or a low-temperature deformation (*44*). By comparing the calculated fcc stability [$\Delta G_{m(fcc\text{-}to\text{-}hcp)}$] of the

screened alloys with $Co_{20}Cr_{20}Fe_{20}Mn_{20}Ni_{20}$ $[\Delta G^{Co_{20}Cr_{20}Fe_{20}Mn_{20}Ni_{20}}_{m(fcc\text{-}to\text{-}hcp)}]$ and $Co_{10}Cr_{10}Fe_{40}Mn_{40}$ $[\Delta G^{Co_{10}Cr_{10}Fe_{40}Mn_{40}}_{m(fcc\text{-}to\text{-}hcp)}]$, the screened alloys are classified as alloys with a less stable fcc and a more stable fcc. The kernel density estimation was generated on the basis of the number of labeled alloys with the Gaussian kernel, and it was applied to determine the alloy probability density distribution of two varying elements. In total, 10 kernel density plots were generated. The plots of Co-Cr, Fe-Ni, Fe-Cr, and Co-Ni are shown in Fig. 3 (A to D), and the rest of plots are shown in fig. S1. In the Fe-Cr and Co-Ni pairs, we can shift the alloys from a more stable fcc to a less stable fcc by increasing the composition of one element and reducing the other element content, as illustrated by the red and black lines in Fig. 3 (C and D, respectively). As a result, we selected seven samples from the Co-Ni (series 1) and Fe-Cr (series 2) series that are purely fcc phase at the homogenization temperature (fig. S2) and have a monotonic reduction in $\Delta G_{m(fcc\text{-}to\text{-}hcp)}$ for further DFT and experimental study (Fig. 3E). The calculated and experimental results of the seven designed alloys and two reference alloys are summarized in Table 1.

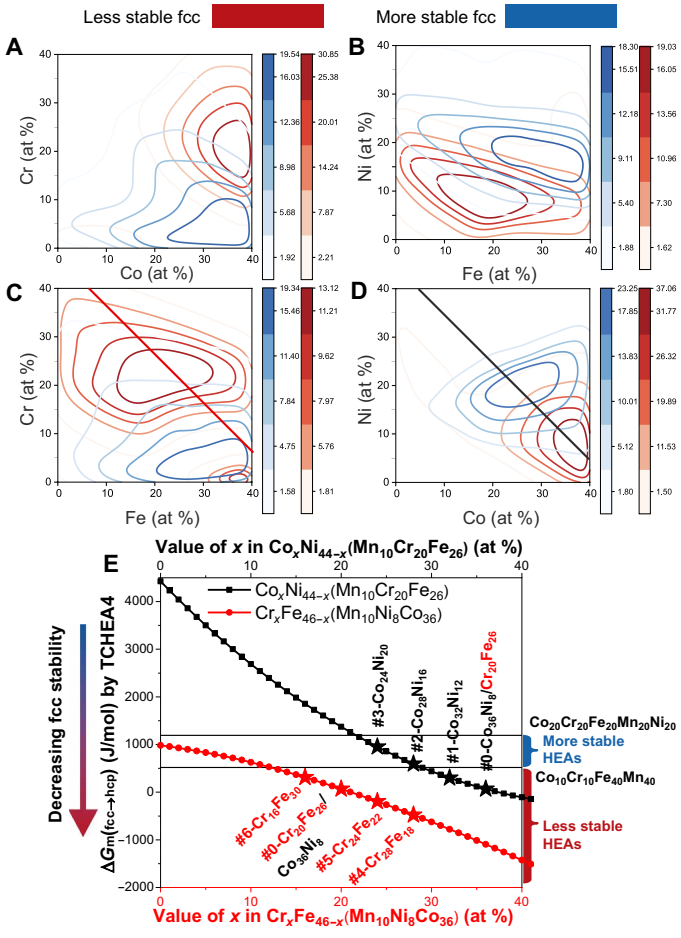

Fig. 3. Design of TRIP/TWIP HEAs using a kernel density plot with different degrees of fcc instability. The screened alloys have been classified as less stable fcc alloy with red color $[\Delta G^{HEAs}_{m(fcc\rightarrow hcp)} < \Delta G^{Co_{10}Cr_{10}Fe_{40}Mn_{40}}_{m(fcc\rightarrow hcp)}]$ and more stable fcc alloy with blue color $[\Delta G^{Co_{10}Cr_{10}Fe_{40}Mn_{40}}_{m(fcc\rightarrow hcp)} < \Delta G^{HEAs}_{m(fcc\rightarrow hcp)} < \Delta G^{Co_{20}Cr_{20}Fe_{20}Mn_{20}Ni_{20}}_{m(fcc\rightarrow hcp)}]$. The kernel density distribution of the two classes of alloys has been plotted with two varying elements. A darker contour line indicates a higher kernel density of the alloys in the composition region. (**A**) Co-Cr pair and (**B**) Fe-Ni pair where the increase of one element and decrease of another element does not lead to the kernel density change from more a stable fcc to a less stable fcc. (**C**) Fe-Cr pair and (**D**) Co-Ni pair where the increase of one element and decrease of another element lead to the kernel density change from a more stable fcc to a less stable fcc. The straight lines indicate the alloy design path. (**E**) The composition and $\Delta G_{m(fcc\text{-}to\text{-}hcp)}$ of the designed alloys and the reference alloys. The red and black curves correspond to the straight lines in (C) and (D) of the same color. The alloys with star marks are selected for further study. Results of other pairs such as Mn-Ni, Fe-Mn, Co-Mn, Fe-Co, Cr-Mn, and Cr-Ni are available in fig. S1.

Prediction of deformation mechanism from first-principles calculations

Figure 4 (A to G) illustrates the initial fcc lattice and different stacking fault structures formed during the passage of a_0/6<112> Shockley partial dislocations. Our model is a nine-layer supercell, where the ISF forms at the boundary of neighboring supercells. After 0.5 $\mathbf{b}_p$ ($\mathbf{b}_p$ is the Burgers vector of Shockley partial dislocation) shear displacement of the upper layers above layer 9, the generalized stacking fault energy reaches the first local maxima. Rice (*45*) named this energy the unstable stacking fault energy (USFE), which is the energy barrier to forming an ISF (*46*). After 1 $\mathbf{b}_p$ displacement, the energy reaches the local minima (ISFE) that can also be determined by experiments such as the TEM or x-ray diffraction. There are two possible further shearing pathways: One is shearing with successive (111) planes. The continuing passage of partial dislocation starts from the 11th plane and will reach a local energy maximum with 1.5 $\mathbf{b}_p$ called the UTFE. The energy difference between UTFE and ISFE is the energy barrier for twin nucleation. The second local minimum energy corresponds to the extrinsic stacking fault (ESF), and it can be viewed as a twin embryo (TE). Repeating the above process in the following layers will result in a larger twin, and the UTFE maintains a similar value (*47*). Previous research has extensively studied the GSFE curve considering the twinning process, and they have proposed many criteria to explain the competition among different deformation mechanisms (*9*, *48*–*50*). However, the mechanism of hcp martensite formation is not well understood, and the energy barrier for TRIP has not been studied using the DFT approach. On the basis of reported experimental observations (*29*, *31*), we propose that another possible shearing path is partial dislocation shearing on every other (111) plane, where the passage of the partial dislocation starts from the 12th layer. As a result, the local minimum energy structure is a martensite embryo (ME), and the energy peak at 1.5 $\mathbf{b}_p$ is defined as the UMFE. The energy difference between UMFE and ISFE is the energy barrier for ME formation. The energies corresponding to the atomic configuration shown in Fig. 4 (A to G) for the two reference alloys and the seven designed alloys are presented in Fig. 4H. We find that the USFE and UTFE are similar for all studied alloys, while the UMFE is different from UTFE. Because the deformation mechanism is favorable when the energy barrier is low, we hypothesize that martensitic phase transformation prevails when UMFE (dashed curves and open symbols such as point F in Fig. 4H) is smaller than UTFE (solid curves and solid symbols such as point D in Fig. 4H), and deformation twinning dominates if the UMFE is larger than the UTFE. Such predictions for the designed alloy and two reference alloys are listed in Table 1.

Experimental verification and TRIP/TWIP mechanism analysis

The seven designed alloys were prepared by arc melting and homogenized at 1200°C, followed by water quenching. It has been found that the grain size of all samples is similar and larger than 100 μm (fig. S3), which does not contribute a high-strengthening mechanism based on the Hall-Petch equation. Figure 5 summarizes the microstructure

Table 1. Summary of selected alloy compositions in atomic %, calculated properties, and experimental observations. at %, atomic %.

Label	Alloy composition (at %)	Phases at 1200°C	$\Delta G_{m(fcc\text{-}to\text{-}hcp)}$ at 20°C (J/mol)	Phase at room temperature		Dominant secondary deformation mechanism	
				CALPHAD	Experiments	DFT	Experiments
Reference alloys from literature							
Ref-1	$Co_{20}Cr_{20}Fe_{20}Mn_{20}Ni_{20}$	fcc	1193	fcc	fcc	TWIP	TWIP [tensile, 77 K (*10*); cold draw, 293 K (*42*)]
Ref-2	$Co_{10}Cr_{10}Fe_{40}Mn_{40}$	fcc orfcc + σ	519	fcc or fcc + σ*	fcc	TWIP	TWIP [tensile, 293 K (*26*)]
Series 1, increasing Ni, decreasing Co							
#0-$Co_{36}Ni_8$/$Cr_{20}Fe_{26}$	$Co_{36}Cr_{20}Fe_{26}Mn_{10}Ni_8$	fcc	67	fcc	fcc	TRIP	TRIP
#1-$Co_{32}Ni_{12}$	$Co_{32}Cr_{20}Fe_{26}Mn_{10}Ni_{12}$	fcc	300	fcc	fcc	TWIP	TWIP
#2-$Co_{28}Ni_{16}$	$Co_{28}Cr_{20}Fe_{26}Mn_{10}Ni_{16}$	fcc	593	fcc	fcc	TWIP	TWIP
#3-$Co_{24}Ni_{20}$	$Co_{24}Cr_{20}Fe_{26}Mn_{10}Ni_{20}$	fcc	952	fcc	fcc	TWIP	TWIP
Series 2, increasing Cr, decreasing Fe							
#4-$Cr_{28}Fe_{18}$	$Co_{36}Cr_{28}Fe_{18}Mn_{10}Ni_8$	fcc	−478	fcc + hcp	fcc + hcp	TRIP	TRIP
#5-$Cr_{24}Fe_{22}$	$Co_{36}Cr_{24}Fe_{22}Mn_{10}Ni_8$	fcc	−196	fcc + hcp	fcc + hcp	TRIP	TRIP
#0-$Cr_{20}Fe_{26}$/$Co_{36}Ni_8$	$Co_{36}Cr_{20}Fe_{26}Mn_{10}Ni_8$	fcc	67	fcc	fcc	TRIP	TRIP
#6-$Cr_{16}Fe_{30}$	$Co_{36}Cr_{16}Fe_{30}Mn_{10}Ni_8$	fcc	310	fcc	fcc + hcp	TRIP	TRIP

*The CALPHAD predicts the high-temperature phase to be fcc and σ due to the slow formation of σ; the phase is taken as fcc or fcc + σ.

of the homogenized and cold-rolled samples characterized by electron backscatter diffraction (EBSD). The phase fractions before and after deformation are listed in table S3. On the basis of Fig. 5 (A1 to G1), the $Co_xCr_{44-x}Fe_{26}Mn_{10}Ni_8$ (x = 36, 32, 28, and 24) alloys are fcc single-phase HEAs, and the $Co_{36}Cr_xFe_{46-x}Mn_{10}Ni_8$ (x = 28, 24, and 16) alloys are fcc + hcp dual-phase HEAs. From Table 1, it is evident that the predicted and observed phases are in good agreement for six of the seven designed alloys, indicating that the phase screening strategy in this work is reliable. By comparing the phase map of homogenized (Fig. 5, A1 to G1) and deformed samples (Fig. 5, A3 to G3), we find that all designed alloys show the existence of a deformation-induced hcp martensite and a minor body-centered cubic (bcc) martensite. Moreover, the $Co_{36}Cr_xFe_{46-x}Mn_{10}Ni_8$ (x = 28, 24, 20, and 16) samples show a noticeable increase in the hcp phase fraction after deformation without any twin formation. This phenomenon implies that the martensitic transformation is the dominant deformation mechanism besides the dislocation glide in these alloys. On the other hand, the $Co_xCr_{44-x}Fe_{26}Mn_{10}Ni_8$ (x = 32, 28, and 24) HEAs show the Σ3 twin boundaries in grain boundary maps (red lines in Fig. 5, B5 to D5) and limited hcp formation when compared with TRIP-dominant alloys. This result suggests that twinning dominates during the deformation of these alloys, and we have labeled them as the TWIP-dominant alloys. Figure 5 (A6 to G6) shows the kernel average misorientation (KAM) maps for the deformed samples. The grain, twin, and phase boundaries show higher KAM values, indicating a higher density of geometrically necessary dislocations (*51*). By comparing these phase maps (Fig. 5, A3 to G3), it is noticed that the bcc phase usually forms at the intersection between hcp phases with a very high KAM value. Such a microstructure confirms that the hcp phase is the precursor for bcc martensite formation, which agrees with the previous study results (*52*). The deformation mechanisms confirmed with EBSD are also summarized in Table 1, and they agree with the DFT prediction.

High-resolution TEM (HRTEM) was performed to identify the atomic structures of the 20% compressed HEAs and verify the dominant deformation mechanisms (Fig. 6). As shown in Fig. 6 (A2), the stacking sequence of the {001} atomic plane follows the ABAB pattern, confirming its hcp stacking nature, which is in direct contrast to the ABCABC stacking of the fcc structure. Moreover, Fig. 6 (A3) shows that the fast Fourier transformation (FFT) of Fig. 6 (A2) matches the simulated hcp diffraction pattern (fig. S4), which further confirms that the sample #0-$Co_{36}Ni_8$/$Cr_{20}Fe_{26}$ shows martensite phase transformation after deformation. Besides the deformation via TRIP, this alloy also displays the twin structure, and the twin boundary is highlighted by a white line in Fig. 6 (B2). The red and blue atomic layers correspond to the FFT in Fig. 6 (B3) with the same color. Although this sample shows a deformation-introduced twin and an hcp structure at a low strain, only hcp phases are identified after 60% deformation using EBSD (Fig. 5A). This result proves that martensitic transformation is the preferred deformation mechanism compared with twinning in this alloy. On the contrary, twins were observed in sample #1-$Co_{32}Ni_{12}$ when the strain was 20%, while no hcp was detected throughout the TEM sample. The EBSD reveals a large amount of twin and hcp after the 60% deformation (Fig. 5B), indicating that twinning is the dominant deformation mechanism at the early deformation, and it also operates at a high-strain level. Therefore, the above HRTEM study strengthens our determination of the TRIP- and TWIP-dominant alloys.

Statistical analysis and verification

To understand the correlation among alloying elements, deformation mechanisms, stacking fault energies, and the previously proposed

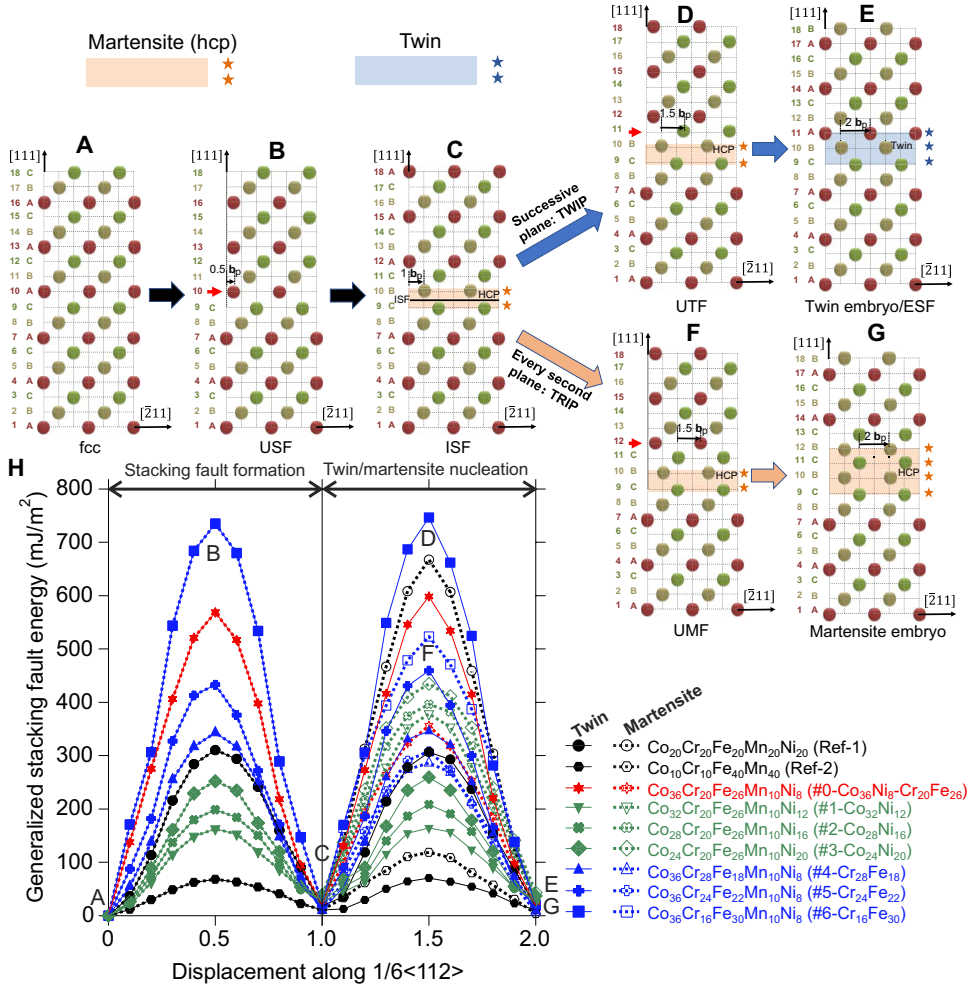

Fig. 4. Calculation of stacking fault energies for the martensite and twin formation and the corresponding atomic configuration. Atomic configuration of (**A**) fcc structure with the ABCABC stacking sequence, (**B**) USF, (**C**) ISF, (**D**) UTF, (**E**) TE, or ESF, (**F**) UMF, and (**G**) ME. Red, brown, and green dots represent atoms in fcc alloys corresponding to the (A) to (C) layers, respectively. The orange square shaded area and orange stars (C, D, F, and G) represent the atomic layers as the hcp phase the atomic layers as the hcp phase. The blue square shaded area and blue stars (E) represent a twin structure a twin structure. All atomic structures are formed through the shear displacement with a Shockley partial dislocation $\mathbf{b}_p = a_0/6<112>$. (**H**) The calculated stacking fault energies of two reference alloys and seven designed alloys using DFT. The local minima and maxima noted with A to G are the energies that correspond to the structure shown in subfigures (A) to (G), respectively. A, energy of fcc structure; B, USF energy (i.e., USFE); C, ISFE; D, UTFE; E, TEE/ESFE; F, UMFE; and G, MEE.

deformation mechanism criteria, we calculated three correlation coefficients on the basis of the variable type and visualized them as a heatmap (Fig. 7). The correlation coefficient ranges from −1 to 1, where 1 represents a perfect positive correlation, 0 corresponds to no monotonic correlation, and −1 gives a perfect negative correlation between the parameter pair. We focus on the statistically significant results with a *p*-value smaller than 0.05. On the basis of the heatmap, we can study the correlation between composition and the stacking fault energies. Co has a strong positive correlation with USFE and UTFE, which implies that Co increases the energy barrier for stacking fault and twin formation. Furthermore, Co decreases ISFE, ESF energy (ESFE)/TE energy (TEE), UMFE, and ME energy (MEE), although the effect is not statistically significant. This observation is consistent with the previous study, suggesting that adding Co can decrease the ISFE and shift the deformation mechanism from twinning to martensitic transformation (*48*). However, it is noted that higher Co content leads to a higher USFE, which may limit the formation of stacking fault that serves as the precursor for the martensite and twin formation. Another important element is Ni, which exhibits a strong effect on increasing the ISFE, ESFE/TEE, UMFE, and MEE. Therefore, while Ni has a minor impact on the twinning energy barrier, its content must be limited to promote the TRIP effect. The findings of the effect of Ni on different stacking fault energies offer a fundamental explanation to the literature-reported phenomenon (*53*) that adding Ni changes the deformation mechanism from martensitic transformation to twinning. As we have proposed, the competition between twinning and martensitic transformation is governed by the energy barriers, such as UTFE-ISFE and UMFE-ISFE. These criteria can be simplified by comparing the values of UTFE and UMFE to predict the dominant deformation mechanism besides the dislocation glide. The condition UMFE < UTFE has a strong positive correlation with TRIP and a strong negative correlation with TWIP. These results suggest that the UMFE < UTFE criterion can predict the deformation mechanism

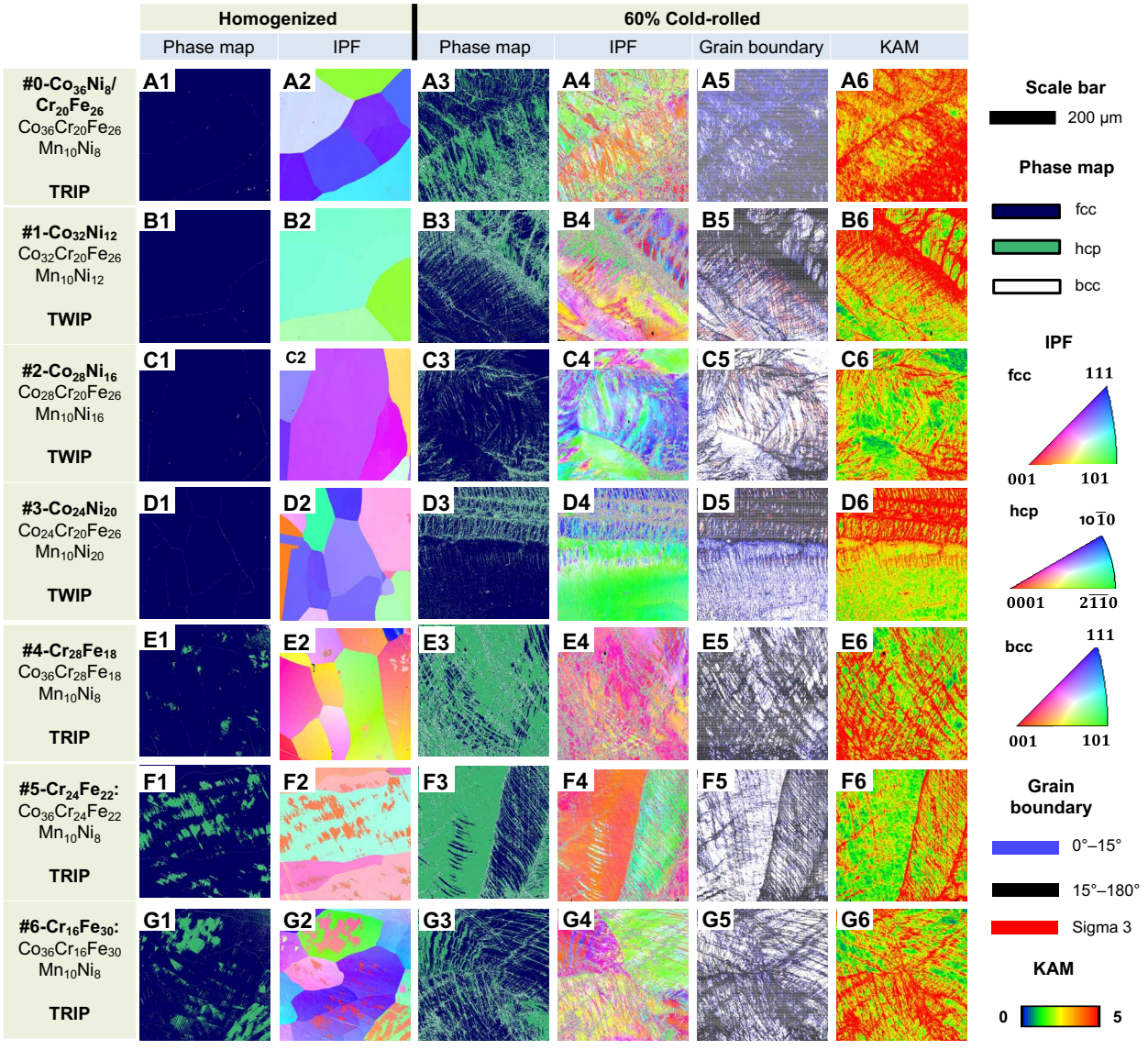

Fig. 5. EBSD characterization of designed alloys. Microstructures of (**A**) $Co_{36}Cr_{20}Fe_{26}Mn_{10}Ni_8$, (**B**) $Co_{32}Cr_{20}Fe_{26}Mn_{10}Ni_{12}$, (**C**) $Co_{28}Cr_{20}Fe_{26}Mn_{10}Ni_{16}$, (**D**) $Co_{24}Cr_{20}Fe_{26}Mn_{10}Ni_{20}$, (**E**) $Co_{36}Cr_{28}Fe_{18}Mn_{10}Ni_8$, (**F**) $Co_{36}Cr_{24}Fe_{22}Mn_{10}Ni_8$, (**G**) and $Co_{36}Cr_{16}Fe_{30}Mn_{10}Ni_8$. Column (1) is the phase map, and column (2) is the inverse pole figure (IPF) map of the homogenized samples. Column (3) is the phase map, column (4) is the IPF map, column (5) grain is the boundary map, and column (6) is the kernel average misorientation (KAM) map of the samples after cold rolling. The legends for all figures and the scale bar are listed on the right side of the figure.

accurately. On the contrary, the parameters used in previous studies, such as ISFE (*48*) and twinnability (*49*), do not show a statistically significant correlation with the deformation mechanisms. They cannot accurately predict the competition between twinning and martensitic transformation due to the inappropriate estimation martensitic transformation energy barrier. A detailed description of previous criteria (*9*, *48*–*50*) and their limitation is available in Supplementary Text and table S4.

To better understand the deformation mechanisms and stacking fault energies, we compared the local minimum energies ISFE, ESFE, and MEE in Fig. 8 (A1) and the energy barriers USFE, UTFE-ISFE, and UMFE-ISFE in Fig. 8 (B1). We also plotted the hardness of the homogenized and deformed samples along with the hardness values reported in the literature for Ref-1 ($Co_{20}Cr_{20}Fe_{20}Mn_{20}Ni_{20}$) (*42*, *54*–*59*) and Ref-2 ($Co_{10}Cr_{10}Fe_{40}Mn_{40}$) (*60*) alloys (Fig. 8, C1). All local minimum energies are positive and smaller than 50 mJ/m^2, which is much lower than the energy barriers. Alloys with an increased Cr and Co content show a lower ISFE, which agrees with the thermodynamic model prediction of fcc instability in Fig. 3E. However, while the CALPHAD-based thermodynamic model shows that all the designed alloys have a lower fcc stability than the Ref-1 alloy, the DFT calculations show that some designed alloys have a higher ISFE, implying that these alloys have a higher fcc stability than the Ref-1 alloy. Such discrepancies can be reduced by introducing a more advanced thermodynamic model considering interfacial energy and improving thermodynamic databases (*25*, *61*). The alloys noted as TRIP dominant have a lower MEE than the ISFE and ESFE/TEE, indicating that the martensite formation introduces less energy into the system than the formation of stacking faults or twins. The TWIP-dominant alloys also have a lower ESFE/TEE,

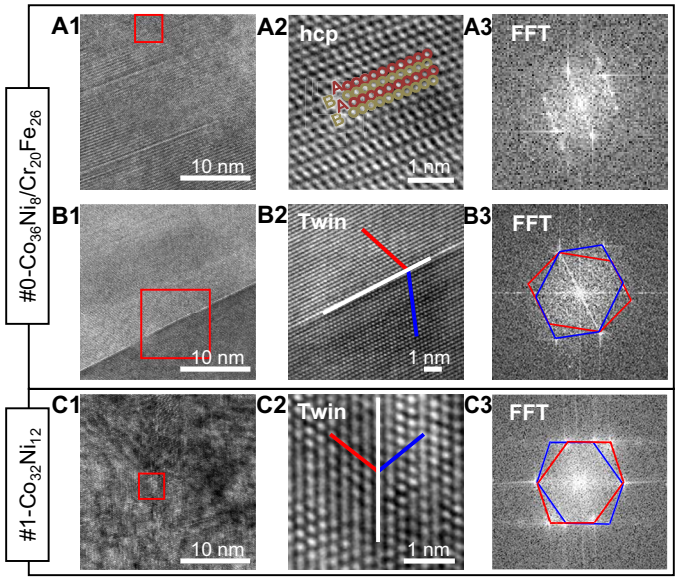

Fig. 6. HRTEM characterization of the samples with a ε = 20% compression. (**A**) and (**B**) are the hcp and twin structures of the TRIP-dominant alloy #0-$Co_{36}Ni_8$/$Cr_{20}Fe_{26}$, respectively. (**C**) shows the twin structure of the TWIP-dominant alloy #1-$Co_{32}Ni_{12}$. Column (1) is the HRTEM that shows the larger area of samples (25 × 25 nm). Column (2) is the small area in the red box in column 1. Column (3) is the diffractogram corresponding to column 2. Zone axes are [100] for the hcp structure and [110] for the fcc structure.

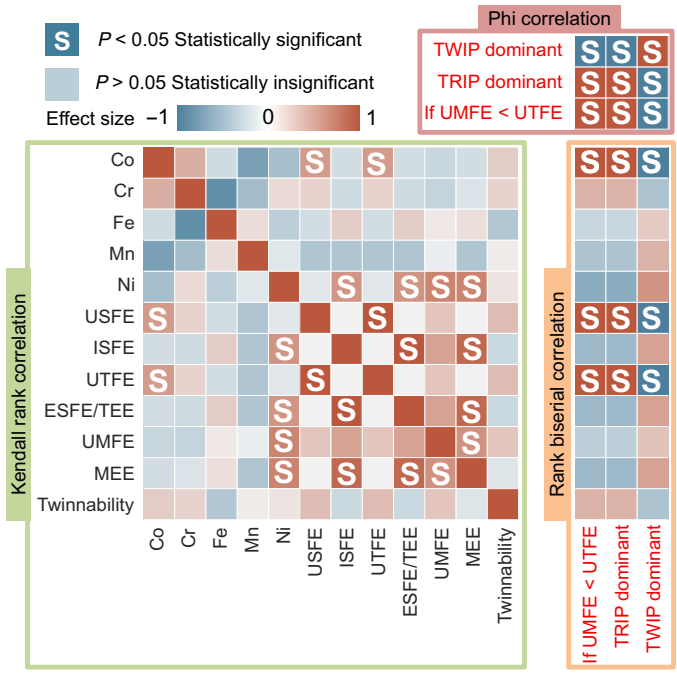

Fig. 7. Correlation coefficient heat map of features and their relationship with TRIP and TWIP. Features in red font are the binary variables, while features in black font are continuous variables. The Phi coefficient (red box), Kendall rank correlation coefficient (green box), and rank biserial correlation coefficient (orange box) as well as *p*-values are calculated for binary-binary, continuous-continuous, and binary-continuous parameter pairs. The red/blue color bar describes the correlation effect size, which indicates a positive/negative relationship between two features, and the darker color means the stronger relationship. Statistically significant results with a $P < 0.05$ are marked with white S. The correlation significances between elements are not included for simplicity. The features can be divided into several categories: Composition (Co, Cr, Fe, Mn, and Ni), DFT-calculated features (USFE, ISFE, UTFE, ESFE, UMFE, and MNE), literature-reported criteria for determining deformation mechanism (twinnability) (*49*), criteria for determining the TRIP/TWIP proposed in this work (if UMFE < UTFE), and the experimentally observed deformation mechanism (TRIP dominant and TWIP dominant).

suggesting a relatively stable twin structure, except for the Ref-2 alloy. Moreover, we have plotted two dashed horizontal lines (Fig. 8, A1) at 20 and 40 mJ/m^2 that are widely adopted as the ISFE upper limits for TRIP and TWIP, respectively (*25*). However, the TRIP-dominant $Co_{36}Cr_xFe_{46-x}Mn_{10}Ni_8$ (x = 16, 20) alloys have an ISFE higher than 20 mJ/m^2, and the TWIP-dominant Ref-1 and Ref-2 alloys exhibit a much lower ISFE. Instead, the martensitic transformation energy barrier (UMFE-ISFE) for TRIP-dominant alloys is much smaller than the stacking fault and the twin formation energy barriers (USFE and UTFE-ISFE). We found that the TRIP-dominant HEAs have higher hardness compared to the TWIP-dominant HEAs. Moreover, the hardness increased after deformation, showing a high-strain hardening effect, and the hardness of the cold-rolled sample tends to decrease with the higher energy barriers for martensite/twin formation.

The results are summarized in the contingency tables embedded in Fig. 8 (A2 and B2) to elucidate the correlation between fault energies and deformation mechanisms. All samples have a low ISFE that is lower than 40 mJ/m^2. This implies that a low ISFE, i.e., low fcc stability, is favorable for introducing secondary deformation mechanisms, such as martensitic transformation and twinning. However, we find that only two of the four TRIP-dominant alloys show an ISFE smaller than 20 mJ/m^2, and three of the five TWIP alloys have an ISFE that lies within the range of 20 to 40 mJ/m^2, which means that the accuracy of this criteria is only about 56%. On the contrary, the accuracy of our model for predicting the deformation mechanism, based on the UMFE-ISFE and UTFE-ISFE relationships, is 100%. Our finding proves that the UMFE-ISFE and UTFE-ISFE, rather than ISFE, should be used as a more general criterion to determine the deformation mechanisms in HEAs.

UMFE/UTFE criteria accuracy for steels

To examine whether the proposed UMFE/UTFE criterion is applicable for other types of alloys, we performed DFT calculations of the different fault energies for literature-reported TRIP or TWIP steels (table S5) (*62*–*65*). The ISFE of TWIP steel (*62*) is calculated to be −289.2 mJ/m^2, and hence, we cannot predict the deformation mechanism based on the calculated ISFE. However, its UTFE (107.3 mJ/m^2) is much smaller than the UMFE (243.6 mJ/m^2), which indicates that the energy barrier for twinning is lower than martensitic transformation. In the high-Mn steel $Mn_{23.7}Al_{5.2}Si_{5.5}Fe_{65.6}$, where both twinning and martensitic transformation operate during deformation (*63*), the UTFE and UMFE are 317.4 and 329.6 mJ/m^2, respectively. The similar energy barriers explain well the coexistence of TRIP and TWIP. However, it is difficult to infer the deformation mechanisms based on the ISFE, which is 27.8 mJ/m^2. In the four different steels tested in this work, the ISFE criterion cannot explain the deformation mechanisms, while all experimental observations can be explained by using the twinning and martensitic transformation energy barriers proposed in this work.

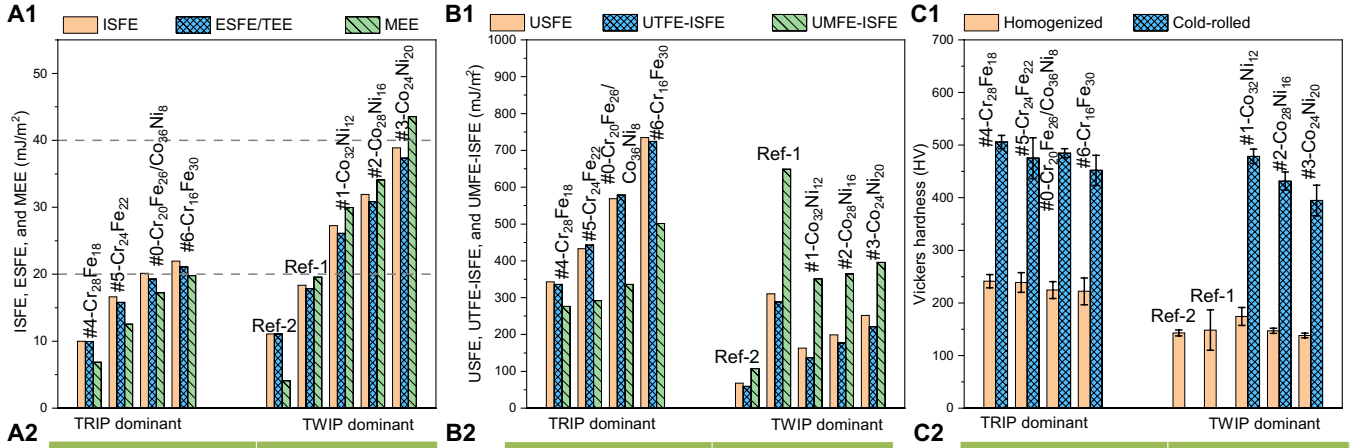

A2

Nine alloys	ISFE range (mJ/m²)	
Deformation type	<20	20–40
TRIP	2	2
TWIP	2	3

B2

Nine alloys	UMFE < UTFE	
Deformation type	True	False
TRIP	4	0
TWIP	0	5

C2

Nine alloys	High hardness	
Deformation type	True	False
TRIP	4	0
TWIP	0	5

Fig. 8. Details of fault energies, deformation mechanism, and hardness. (**A**) ISFE, ESFE/TEE, and MEE of all designed alloys and two reference alloys; the dashed lines are 20 and 40 mJ/m^2 corresponding to the upper limit of TRIP and TWIP, respectively. (**B**) USFE, UTFE, UMFE of all designed alloys and two reference alloys. (**C**) The hardness of homogenized and cold-rolled samples. The average and sample SD for the designed alloys' hardness is calculated on the basis of 10 indents for each sample. The hardness and SD of Ref-1 ($Co_{20}Cr_{20}Fe_{20}Mn_{20}Ni_{20}$) are taken from the literature (*42*, *54*–*59*). The hardness and SD of Ref-2 ($Co_{10}Cr_{10}Fe_{40}Mn_{40}$) are adopted from (*60*). (A1 to C1) Plots and (A2 to C2) contingency tables summarize the relationships among deformation mechanisms (TRIP/TWIP) with an ISF range, unstable fault energies, and hardness before and after cold rolling, respectively.

DISCUSSION

In this work, we found that processing history and athermal phase transformations should be considered in addition to the chemical composition for an accurate phase prediction of HEAs. Moreover, we also showed that, while a low ISFE is favorable for the secondary deformation mechanism, it cannot predict whether martensitic transformation or twinning is the dominant deformation mechanism. Instead, the difference between UMFE/UTFE and ISFE is the energy barrier that determines the competition between twinning and martensitic transformation. Last, seven HEAs with TRIP and TWIP have been designed and produced to demonstrate the effectiveness of our design approach by combining rapid CALPHAD screening of phase stability and accurate DFT-based prediction of the deformation mechanism.

It is noted that we did not test the tensile properties, which is more appropriate to evaluate the mechanical properties of the designed HEAs and may help us to select the best HEA with potential applications. Although the systematic mechanical property evaluation is beneficial, the target of this work, which is to provide guidance for calculating the energy associated with martensitic transformation, discover the actual energy barrier for TRIP/TWIP, and propose a design paradigm for the community to accelerate the discovery of TRIP/TWIP in a wide spectrum of alloys, has been achieved.

MATERIALS AND METHODS

Calculation

Thermodynamic screening

The CALPHAD approach was used for thermodynamic phase screening. The calculations were performed using the TC-Python toolkit from the Thermo-Calc software with the TCHEA4 database (*66*). The searched composition space is 0 < Co ≤ 40 atomic (at %), 0 < Cr ≤ 40 at %, 0 < Mn ≤ 40 at %, and 0 < Ni ≤ 40 at %, with Fe as the balance element and its upper limit was set to be 40 at %.

First-principles calculations

DFT calculations with the exact muffin-tin orbital (EMTO) (*67*) method were performed to calculate the planar defect energies of the studied alloys. As an improved screened Korringa-Kohn-Rostoker method, the EMTO method uses optimized overlapping muffin-tin potential spheres to represent the exact one-electron potential (*68*). The one-electron equations were solved within the scalar relativistic approximation and the soft-core scheme. The chemical disorder of the HEA was treated with the coherent-potential approximation (*69*). The Perdew-Burke-Ernzerhof–generalized gradient approximation (*70*) was used to approximate the exchange-correlation energy. The EMTO Green's function was calculated self-consistently for 16 complex energy points distributed exponentially (*71*). On the basis of the experimental observation that the Curie temperatures of these systems are normally lower than room temperature (*72*), the results from the paramagnetic (PM) state are chosen as a more efficient approach (*73*). The initial magnetic field was described by the disordered local magnetic moment approach (*74*), each element was regarded as two separate parts with up and down spins. The stacking fault energy is calculated as the energy difference between the ideal fcc lattice and the modified lattice containing the stacking fault. To be specific, sliding one layer at different distances and fixing the relative positions of other layers will obtain a series of stacking fault energy. The sliding was modeled using tilted supercells from applying a partial dislocation Burgers vector $n\,\mathbf{b}_p$ ($\mathbf{b}_p = a_0$<112>/6, where a_0 is the lattice constant, and n is increased by steps of 0.1 on the original supercell, which is parallel to the stacking direction) (perpendicular to the stacking fault plane) (*75*). A model of successive nine (111) planes (*47*) was used in this work to eliminate the

interaction between stacking fault layers and ensure convergence. For each 0.1 $\mathbf{b}_p$ sliding, the interlayer distances between the layers containing the stacking fault were optimized (*75*), while other interlayer distances were fixed. The *k*-mesh was carefully tested for convergence, and the $12 \times 24 \times 3$ mesh was adopted for all calculations.

Correlation analysis

All statistical analyses were coded using SciPy (*76*) and scikit-learn (*77*). For two continuous variables, the coefficient and associated *p*-value of Pearson correlation and Kendall rank correlation were calculated using SciPy (*76*). For two binary variable pairs, the Phi coefficient was calculated using the Matthew correlation coefficient implemented in scikit-learn (*77*). Furthermore, the *p*-value was calculated using Fisher's exact test available in SciPy. For one binary variable and one continuous variable pair, the *p*-value was obtained from the Mann-Whitney rank test in SciPy, and the effect size was calculated on the basis of the method proposed by Kerby (*78*).

Experiments

Sample preparation, heat treatment, and deformation

High-purity elements [Mn, 99.98 weight % (wt %); Ni, 99.98 wt %; Cr, 99.95 wt %; Fe, 99.99 wt %; and Co, 99.9 wt %] were weighted in a high-precision balance (± 0.1 mg) in accordance with the designed compositions indicated in Table 1. We added an extra 2 wt % of Mn to all compositions to compensate for the expected Mn evaporation losses during casting. Forty grams of ingot for series one alloys and 10 g of ingot for the series two alloys were cast in an arc melter (ABJ-338 manufactured, Materials Research Furnaces Inc., USA) operated with a copper crucible and under an argon atmosphere. Pure zirconium was used to remove any remnant oxygen present in the casting chamber. Moreover, each alloy was remelted at least three times to ensure a homogeneous ingot with less than 0.5% weight loss. Afterward, disc- and rectangular-shaped samples cut from the arc-melted ingots were encapsulated in quartz tubes, purged under vacuum, and backfilled with argon gas. Homogenization was carried out at 1200°C for 1 hour followed by ice water quenching. Disc-shaped samples were used to study the microstructure without deformation, while the rectangular-shaped samples were dedicated for cold rolling. A 60% thickness reduction in a single pass during cold rolling was designed to be imposed in all alloys to ensure that large hcp plates or twins could form. $Co_{32}Cr_{20}Fe_{26}Mn_{10}Ni_{12}$ and $Co_{36}Cr_{20}Fe_{26}Mn_{10}Ni_8$ alloys were machined to cylinder shape with a diameter of 5 mm and a height of 10 mm. The cylinder samples were compressed for $\varepsilon = 20\%$, with a strain rate of 10^{-3} s^{-1} on an MTS Landmark Servohydraulic Test System.

Microstructure characterization

Both undeformed and deformed samples were hot mounted, ground, and polished to a mirror-like finish using a 0.1-μm diamond and 0.02-μm silica particle suspension solutions. Microstructure characterization was conducted using a FEI Scios DualBeam scanning electron microscope. Energy-dispersive spectroscopy was carried out to ensure that no element segregation was present after homogenization. Furthermore, EBSD was performed for a 400 μm by 400 μm area with a step size of 0.75 μm for both sets of samples and analyzed with the TexSEM Laboratories (TSL) orientation imaging microscopy (OIM) Analysis v8 software. Thin-film TEM samples were prepared with a Fischione Model 110 twin-jet electropolisher maintained at a temperature range of −30° to −20°C, using an etching electrolyte composed of 10 volume % perchloric acid and 90 volume % methanol. Those samples were subsequently characterized with HRTEM to investigate the microstructure and the early deformation stage using a JEOL JEM-2100F 200 kV TEM equipped with a Schottky field-emission gun.

Microhardness

Vickers microhardness measurements were conducted in all samples using an AMH55 with LM310AT Microindenter, LECO Corporation automatic hardness tester with 100 gram-force and 10-s dwelling time. Reported values correspond to an average and SD of 10 readings.

SUPPLEMENTARY MATERIALS

Supplementary material for this article is available at https://science.org/doi/10.1126/sciadv.abo7333

REFERENCES AND NOTES

1. R. O. Ritchie, The conflicts between strength and toughness. *Nat. Mater.* **10**, 817–822 (2011).
2. Y. Wei, Y. Li, L. Zhu, Y. Liu, X. Lei, G. Wang, Y. Wu, Z. Mi, J. Liu, H. Wang, Evading the strength–ductility trade-off dilemma in steel through gradient hierarchical nanotwins. *Nat. Commun.* **5**, 3580 (2014).
3. Z. Li, K. G. Pradeep, Y. Deng, D. Raabe, C. C. Tasan, Metastable high-entropy dual-phase alloys overcome the strength-ductility trade-off. *Nature* **534**, 227–230 (2016).
4. J. W. Bae, J. B. Seol, J. Moon, S. S. Sohn, M. J. Jang, H. Y. Um, B.-J. Lee, H. S. Kim, Exceptional phase-transformation strengthening of ferrous medium-entropy alloys at cryogenic temperatures. *Acta Mater.* **161**, 388–399 (2018).
5. O. Grässel, L. Krüger, G. Frommeyer, L. W. Meyer, High strength Fe-Mn-(Al, Si) TRIP/TWIP steels development-properties-application. *Int. J. Plast.* **16**, 1391–1409 (2000).
6. B. X. Cao, C. Wang, T. Yang, C. T. Liu, Cocktail effects in understanding the stability and properties of face-centered-cubic high-entropy alloys at ambient and cryogenic temperatures. *Scr. Mater.* **187**, 250–255 (2020).
7. J. Yeh, S. Chen, S. Lin, J. Gan, T. Chin, T. Shun, C. Tsau, S. Chang, Nanostructured high-entropy alloys with multiple principal elements: Novel alloy design concepts and outcomes. *Adv. Eng. Mater.* **6**, 299–303 (2004).
8. Y. Deng, C. C. Tasan, K. G. Pradeep, H. Springer, A. Kostka, D. Raabe, Design of a twinning-induced plasticity high entropy alloy. *Acta Mater.* **94**, 124–133 (2015).
9. S. Huang, H. Huang, W. Li, D. Kim, S. Lu, X. Li, E. Holmström, S. K. Kwon, L. Vitos, Twinning in metastable high-entropy alloys. *Nat. Commun.* **9**, 2381 (2018).
10. B. Gludovatz, A. Hohenwarter, D. Catoor, E. H. Chang, E. P. George, R. O. Ritchie, A fracture-resistant high-entropy alloy for cryogenic applications. *Science* **345**, 1153–1158 (2014).
11. S. H. Shim, H. Pouraliakbar, S. I. Hong, High strength dual fcc phase CoCuFeMnNi high-entropy alloy wires with dislocation wall boundaries stabilized by phase boundaries. *Mater. Sci. Eng. A* **825**, 141875 (2021).
12. Y. Zhang, T. T. Zuo, Z. Tang, M. C. Gao, K. A. Dahmen, P. K. Liaw, Z. P. Lu, Microstructures and properties of high-entropy alloys. *Prog. Mater. Sci.* **61**, 1–93 (2014).
13. W.-Y. Ching, S. San, J. Brechtl, R. Sakidja, M. Zhang, P. K. Liaw, Fundamental electronic structure and multiatomic bonding in 13 biocompatible high-entropy alloys. *npj Comput. Mater.* **6**, 45 (2020).
14. E. P. George, W. A. Curtin, C. C. Tasan, High entropy alloys: A focused review of mechanical properties and deformation mechanisms. *Acta Mater.* **188**, 435–474 (2020).
15. G. B. Olson, Computational design of hierarchically structured materials. *Science* **277**, 1237–1242 (1997).
16. G. B. Olson, C. J. Kuehmann, Materials genomics: From CALPHAD to flight. *Scr. Mater.* **70**, 25–30 (2014).
17. Y. Zhang, C. Wen, C. Wang, S. Antonov, D. Xue, Y. Bai, Y. Su, Phase prediction in high entropy alloys with a rational selection of materials descriptors and machine learning models. *Acta Mater.* **185**, 528–539 (2020).
18. Y. Zhang, Z. P. Lu, S. G. Ma, P. K. Liaw, Z. Tang, Y. Q. Cheng, M. C. Gao, Guidelines in predicting phase formation of high-entropy alloys. *MRS Commun.* **4**, 57–62 (2014).
19. Z. Pei, J. Yin, J. A. Hawk, D. E. Alman, M. C. Gao, Machine-learning informed prediction of high-entropy solid solution formation: Beyond the Hume-Rothery rules. *npj Comput. Mater.* **6**, 50 (2020).
20. W. Huang, P. Martin, H. L. Zhuang, Machine-learning phase prediction of high-entropy alloys. *Acta Mater.* **169**, 225–236 (2019).
21. E. P. George, D. Raabe, R. O. Ritchie, High-entropy alloys. *Nat. Rev. Mater.* **4**, 515–534 (2019).
22. A. Abu-Odeh, E. Galvan, T. Kirk, H. Mao, Q. Chen, P. Mason, R. Malak, R. Arróyave, Efficient exploration of the high entropy alloy composition-phase space. *Acta Mater.* **152**, 41–57 (2018).
23. S. Yang, J. Lu, F. Xing, L. Zhang, Y. Zhong, Revisit the VEC rule in high entropy alloys (HEAs) with high-throughput CALPHAD approach and its applications for material design-A case study with Al-Co-Cr-Fe-Ni system. *Acta Mater.* **192**, 11–19 (2020).

24. M. Shih, J. Miao, M. Mills, M. Ghazisaeidi, Stacking fault energy in concentrated alloys. *Nat. Commun.* **12**, 3590 (2021).
25. X. Wang, W. Xiong, Stacking fault energy prediction for austenitic steels: Thermodynamic modeling vs. machine learning. *Sci. Technol. Adv. Mater.* **21**, 626–634 (2020).
26. S. Picak, J. Liu, C. Hayrettin, W. Nasim, D. Canadinc, K. Xie, Y. I. Chumlyakov, I. V. Kireeva, I. Karaman, Anomalous work hardening behavior of $Fe_{40}Mn_{40}Cr_{10}Co_{10}$ high entropy alloy single crystals deformed by twinning and slip. *Acta Mater.* **181**, 555–569 (2019).
27. Y. H. Zhang, Y. Zhuang, A. Hu, J. J. Kai, C. T. Liu, The origin of negative stacking fault energies and nano-twin formation in face-centered cubic high entropy alloys. *Scr. Mater.* **130**, 96–99 (2017).
28. X. Sun, S. Lu, R. Xie, X. An, W. Li, T. Zhang, C. Liang, X. Ding, Y. Wang, H. Zhang, L. Vitos, Can experiment determine the stacking fault energy of metastable alloys? *Mater. Des.* **199**, 109396 (2021).
29. X. Wu, Z. Li, Z. Rao, Y. Ikeda, B. Dutta, F. Körmann, J. Neugebauer, D. Raabe, Role of magnetic ordering for the design of quinary TWIP-TRIP high entropy alloys. *Phys. Rev. Mater.* **4**, 033601 (2020).
30. G. B. Olson, M. Cohen, Kinetics of strain-induced martensitic nucleation. *Metall. Trans. A.* **6**, 791–795 (1975).
31. H. Fujita, S. Ueda, Stacking faults and f.c.c. (γ) → h.c.p. (ϵ) transformation in 188-type stainless steel. *Acta Metall.* **20**, 759–767 (1972).
32. K. Ishida, Direct estimation of stacking fault energy by thermodynamic analysis. *Phys. Stat. Solidi* **36**, 717–728 (1976).
33. S. F. Liu, Y. Wu, H. T. Wang, J. Y. He, J. B. Liu, C. X. Chen, X. J. Liu, H. Wang, Z. P. Lu, Stacking fault energy of face-centered-cubic high entropy alloys. *Intermetallics* **93**, 269–273 (2018).
34. G. Laplanche, A. Kostka, C. Reinhart, J. Hunfeld, G. Eggeler, E. P. George, Reasons for the superior mechanical properties of medium-entropy CrCoNi compared to high-entropy CrMnFeCoNi. *Acta Mater.* **128**, 292–303 (2017).
35. Y. Wang, B. Liu, K. Yan, M. Wang, S. Kabra, Y.-L. Chiu, D. Dye, P. D. Lee, Y. Liu, B. Cai, Probing deformation mechanisms of a FeCoCrNi high-entropy alloy at 293 and 77 K using in situ neutron diffraction. *Acta Mater.* **154**, 79–89 (2018).
36. B. Cai, B. Liu, S. Kabra, Y. Wang, K. Yan, P. D. Lee, Y. Liu, Deformation mechanisms of Mo alloyed FeCoCrNi high entropy alloy: In situ neutron diffraction. *Acta Mater.* **127**, 471–480 (2017).
37. S. F. Liu, Y. Wu, H. T. Wang, W. T. Lin, Y. Y. Shang, J. B. Liu, K. An, X. J. Liu, H. Wang, Z. P. Lu, Transformation-reinforced high-entropy alloys with superior mechanical properties via tailoring stacking fault energy. *J. Alloys Compd.* **792**, 444–455 (2019).
38. N. L. Okamoto, S. Fujimoto, Y. Kambara, M. Kawamura, Z. M. T. Chen, H. Matsunoshita, K. Tanaka, H. Inui, E. P. George, Size effect, critical resolved shear stress, stacking fault energy, and solid solution strengthening in the CrMnFeCoNi high-entropy alloy. *Sci. Rep.* **6**, 35863 (2016).
39. Z. Wang, I. Baker, Z. Cai, S. Chen, J. D. Poplawsky, W. Guo, The effect of interstitial carbon on the mechanical properties and dislocation substructure evolution in $Fe_{40.4}Ni_{11.3}Mn_{34.8}Al_{7.5}Cr_6$ high entropy alloys. *Acta Mater.* **120**, 228–239 (2016).
40. X. D. Xu, P. Liu, Z. Tang, A. Hirata, S. X. Song, T. G. Nieh, P. K. Liaw, C. T. Liu, M. W. Chen, Transmission electron microscopy characterization of dislocation structure in a face-centered cubic high-entropy alloy $Al_{0.1}$CoCrFeNi. *Acta Mater.* **144**, 107–115 (2018).
41. D. Wei, X. Li, S. Schönecker, J. Jiang, W.-M. Choi, B.-J. Lee, H. S. Kim, A. Chiba, H. Kato, Development of strong and ductile metastable face-centered cubic single-phase high-entropy alloys. *Acta Mater.* **181**, 318–330 (2019).
42. X. Ma, J. Chen, X. Wang, Y. Xu, Y. Xue, Microstructure and mechanical properties of cold drawing CoCrFeMnNi high entropy alloy. *J. Alloys Compd.* **795**, 45–53 (2019).
43. P. Sathiyamoorthi, P. Asghari-Rad, G. M. Karthik, A. Zargaran, H. S. Kim, Unusual strain-induced martensite and absence of conventional grain refinement in twinning induced plasticity high-entropy alloy processed by high-pressure torsion. *Mater. Sci. Eng. A* **803**, 140570 (2021).
44. L. B. Chen, R. Wei, K. Tang, J. Zhang, F. Jiang, J. Sun, Ductile-brittle transition of carbon alloyed Fe40Mn40Co10Cr10 high entropy alloys. *Mater. Lett.* **236**, 416–419 (2019).
45. J. R. Rice, Dislocation nucleation from a crack tip: An analysis based on the Peierls concept. *J. Mech. Phys. Solids* **40**, 239–271 (1992).
46. H. Van Swygenhoven, P. M. Derlet, A. G. Frøseth, Stacking fault energies and slip in nanocrystalline metals. *Nat. Mater.* **3**, 399–403 (2004).
47. S. Kibey, J. B. Liu, D. D. Johnson, H. Sehitoglu, Predicting twinning stress in fcc metals: Linking twin-energy pathways to twin nucleation. *Acta Mater.* **55**, 6843–6851 (2007).
48. D. Wei, X. Li, J. Jiang, W. Heng, Y. Koizumi, W.-M. Choi, B.-J. Lee, H. S. Kim, H. Kato, A. Chiba, Novel Co-rich high performance twinning-induced plasticity (TWIP) and transformation-induced plasticity (TRIP) high-entropy alloys. *Scr. Mater.* **165**, 39–43 (2019).
49. M. B. Kivy, M. A. Zaeem, Generalized stacking fault energies, ductilities, and twinnabilities of CoCrFeNi-based face-centered cubic high entropy alloys. *Scr. Mater.* **139**, 83–86 (2017).
50. W. Li, S. Lu, D. Kim, K. Kokko, S. Hertzman, S. K. Kwon, L. Vitos, First-principles prediction of the deformation modes in austenitic Fe-Cr-Ni alloys. *Appl. Phys. Lett.* **108**, 081903 (2016).
51. M. Calcagnotto, D. Ponge, E. Demir, D. Raabe, Orientation gradients and geometrically necessary dislocations in ultrafine grained dual-phase steels studied by 2D and 3D EBSD. *Mater. Sci. Eng. A* **527**, 2738–2746 (2010).
52. T. H. Lee, E. Shin, C. S. Oh, H. Y. Ha, S. J. Kim, Correlation between stacking fault energy and deformation microstructure in high-interstitial-alloyed austenitic steels. *Acta Mater.* **58**, 3173–3186 (2010).
53. A. Glage, A. Weidner, H. Biermann, Cyclic deformation behaviour of three austenitic cast CrMnNi TRIP/TWIP steels with various Ni content. *Steel Res. Int.* **82**, 1040–1047 (2011).
54. B. Schuh, F. Mendez-Martin, B. Völker, E. P. George, H. Clemens, R. Pippan, A. Hohenwarter, Mechanical properties, microstructure and thermal stability of a nanocrystalline CoCrFeMnNi high-entropy alloy after severe plastic deformation. *Acta Mater.* **96**, 258–268 (2015).
55. A. Heczel, M. Kawasaki, J. L. Lábár, J. Jang, T. G. Langdon, J. Gubicza, Defect structure and hardness in nanocrystalline CoCrFeMnNi high-entropy alloy processed by high-pressure torsion. *J. Alloys Compd.* **711**, 143–154 (2017).
56. G. Laplanche, O. Horst, F. Otto, G. Eggeler, E. P. George, Microstructural evolution of a CoCrFeMnNi high-entropy alloy after swaging and annealing. *J. Alloys Compd.* **647**, 548–557 (2015).
57. E. Abbasi, K. Dehghani, Effect of Nb-C addition on the microstructure and mechanical properties of CoCrFeMnNi high entropy alloys during homogenisation. *Mater. Sci. Eng. A* **753**, 224–231 (2019).
58. J. Joseph, N. Haghdadi, K. Shamlaye, P. Hodgson, M. Barnett, D. Fabijanic, The sliding wear behaviour of CoCrFeMnNi and AlxCoCrFeNi high entropy alloys at elevated temperatures. *Wear* **428–429**, 32–44 (2019).
59. E. Abbasi, K. Dehghani, Hot tensile properties of CoCrFeMnNi(NbC) compositionally complex alloys. *Mater. Sci. Eng. A* **772**, 138771 (2020).
60. L. B. Chen, R. Wei, K. Tang, J. Zhang, F. Jiang, L. He, J. Sun, Heavy carbon alloyed FCC-structured high entropy alloy with excellent combination of strength and ductility. *Mater. Sci. Eng. A* **716**, 150–156 (2018).
61. S. Curtze, V.-T. Kuokkala, A. Oikari, J. Talonen, H. Hänninen, Thermodynamic modeling of the stacking fault energy of austenitic steels. *Acta Mater.* **59**, 1068–1076 (2011).
62. I. Gutierrez-Urrutia, D. Raabe, Dislocation and twin substructure evolution during strain hardening of an Fe-22wt.% Mn-0.6wt.% C TWIP steel observed by electron channeling contrast imaging. *Acta Mater.* **59**, 6449–6462 (2011).
63. D. T. Pierce, J. A. Jiménez, J. Bentley, D. Raabe, J. E. Wittig, The influence of stacking fault energy on the microstructural and strain-hardening evolution of Fe-Mn-Al-Si steels during tensile deformation. *Acta Mater.* **100**, 178–190 (2015).
64. J. Talonen, H. Hänninen, Formation of shear bands and strain-induced martensite during plastic deformation of metastable austenitic stainless steels. *Acta Mater.* **55**, 6108–6118 (2007).
65. Y. J. Yin, J. Q. Sun, J. Guo, X. F. Kan, D. C. Yang, Mechanism of high yield strength and yield ratio of 316 L stainless steel by additive manufacturing. *Mater. Sci. Eng. A* **744**, 773–777 (2019).
66. J.-O. Andersson, T. Helander, L. Höglund, P. Shi, B. Sundman, Thermo-Calc & DICTRA, computational tools for materials science. *CAL* **26**, 273–312 (2002).
67. L. Vitos, *Computational Quantum Mechanics for Materials Engineers: The EMTO Method and Applications* (Springer Science & Business Media, 2007).
68. O. K. Andersen, C. Arcangeli, R. W. Tank, T. Saha-Dasgupta, G. Krier, O. Jepsen, I. Dasgupta, Third-generation TB-LMTO. *MRS Proc.* **491**, 3–34 (1997).
69. B. L. Gyorffy, Coherent-potential approximation for a nonoverlapping-muffin-tin-potential model of random substitutional alloys. *Phys. Rev. B* **5**, 2382–2384 (1972).
70. J. P. Perdew, K. Burke, M. Ernzerhof, Generalized gradient approximation made simple. *Phys. Rev. Lett.* **77**, 3865–3868 (1996).
71. W. Li, S. Lu, Q.-M. Hu, S. K. Kwon, B. Johansson, L. Vitos, Generalized stacking fault energies of alloys. *J. Phys. Condens. Matter* **26**, 265005 (2014).
72. O. Schneeweiss, M. Friák, M. Dudová, D. Holec, M. Šob, D. Kriegner, V. Holý, P. Beran, E. P. George, J. Neugebauer, A. Dlouhy, Magnetic properties of the CrMnFeCoNi high-entropy alloy. *Phys. Rev. B* **96**, 14437 (2017).
73. S. Huang, E. Holmström, O. Eriksson, L. Vitos, Mapping the magnetic transition temperatures for medium-and high-entropy alloys. *Intermetallics* **95**, 80–84 (2018).
74. A. J. Pindor, J. Staunton, G. M. Stocks, H. Winter, Disordered local moment state of magnetic transition metals: A self-consistent KKR CPA calculation. *J. Phys. F Met. Phys.* **13**, 979–989 (1983).
75. L.-Y. Tian, R. Lizárraga, H. Larsson, E. Holmström, L. Vitos, A first principles study of the stacking fault energies for fcc Co-based binary alloys. *Acta Mater.* **136**, 215–223 (2017).
76. P. Virtanen, R. Gommers, T. E. Oliphant, M. Haberland, T. Reddy, D. Cournapeau, E. Burovski, P. Peterson, W. Weckesser, J. Bright, S. J. van der Walt, M. Brett, J. Wilson, K. J. Millman, N. Mayorov, A. R. J. Nelson, E. Jones, R. Kern, E. Larson, C. J. Carey, İ. Polat, Y. Feng, E. W. Moore, J. V. Plas, D. Laxalde, J. Perktold, R. Cimrman, I. Henriksen, E. A. Quintero, C. R. Harris, A. M. Archibald, A. H. Ribeiro, F. Pedregosa, P. van Mulbregt; SciPy 1.0 Contributors, SciPy 1.0: Fundamental algorithms for scientific computing in Python. *Nat. Methods.* **17**, 261–272 (2020).

77. F. Pedregosa, G. Varoquaux, A. Gramfort, V. Michel, B. Thirion, O. Grisel, M. Blondel, P. Prettenhofer, R. Weiss, V. Dubourg, J. Vanderplas, A. Passos, D. Cournapeau, M. Brucher, M. Perrot, É. Duchesnay, scikit-learn: Machine learning in Python. *J. Mach. Learn. Res.* **12**, 2825–2830 (2011).
78. D. S. Kerby, The simple difference formula: An approach to teaching nonparametric correlation. *Compr. Psychol.* **3**, 11-IT (2014).

Acknowledgments: We are grateful for the helpful discussions with N. Sargent and Y. Zhao. **Funding:** This work was supported by the National Science Foundation under grants no. CMMI-2047218 and no. DMR-1945380; the Extreme Science and Engineering Discovery Environment (XSEDE), which is supported by National Science Foundation grant no. ACI-1548562; and the National Energy Research Scientific Computing Center (NERSC), a U.S. Department of Energy Office of Science User Facility located at Lawrence Berkeley National Laboratory, operated under contract no. DE-AC02-05CH11231. Article-processing charges for this article are supported by the University Library System, University of Pittsburgh. **Author contributions:** W.X., W.C., and X.W. conceptualized this work. X.W. and C.L. conducted the calculation. R.R.D.V., H.Z., X.H., S.S., and Y.W. performed the experiments. X.W., C.L., R.R.D.V., and H.Z. investigated the results. X.W. visualized the results. W.X. and W.C. supervised this work. All authors discussed the results and contributed to the writing of the paper. **Competing interests:** The authors declare that they have no competing interests. **Data and materials availability:** All data needed to evaluate the conclusions in the paper are present in the paper and/or the Supplementary Materials.

Submitted 9 March 2022
Accepted 25 July 2022
Published 9 September 2022
10.1126/sciadv.abo7333